THE JOURNAL OF PHYSICAL CHEMISTRY C

Article

pubs.acs.org/JPCC

Surface Stabilizes Ceria in Unexpected Stoichiometry

Reinhard Olbrich,[†,‡] Gustavo E. Murgida,[‡,§,∥] Valeria Ferrari,[§,∥] Clemens Barth,[⊥] Ana M. Llois,[§,∥] Michael Reichling,[*,†] and M. Verónica Ganduglia-Pirovano[*,#]

[†]Fachbereich Physik, Universität Osnabrück, Barbarastr. 7, 49076 Osnabrück, Germany

[§]Departamento de Física de la Materia Condensada, GIyA, CAC−CNEA, 1650 San Martín, Buenos Aires, Argentina

[∥]Consejo Nacional de Investigaciones Científicas y Técnicas - CONICET, C1033AAJ Buenos Aires, Argentina

[⊥]Aix-Marseille University, CNRS, CINaM UMR 7325, 13288 Marseille, France

[#]Instituto de Catálisis y Petroleoquímica, Consejo Superior de Investigaciones Científicas-CSIC, 28049 Madrid, Spain

ABSTRACT: The prototype reducible oxide ceria is known for its rich phase diagram and its ability to absorb and deliver oxygen. The high oxygen storage capacity is the basis for the use of ceria in catalytic and sensor applications where the surface plays a paramount role for device functionality. By direct imaging, we reveal the reconstruction of the ceria (111) surface in five periodic structures representing reduction stages ranging from CeO_2 to Ce_2O_3. Theoretical modeling shows that the $(\sqrt{7} \times 3)$R19.1° reconstruction, representing the previously unknown Ce_3O_5 stoichiometry, is stabilized at the surface but cannot be assigned to a bulk structure. Statistical modeling explains the thermodynamic stability of surface phases depending on the oxygen chemical potential and the coexistence of certain phases over a range of temperatures. These results are crucial for understanding geometric and electronic structure−function correlations in nanostructured ceria and the rational design of novel ceria-based functional systems.

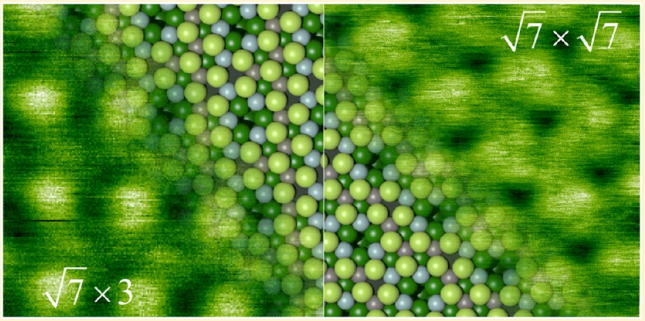

INTRODUCTION

Oxygen mobility in a solid state material is the basis of numerous processes in electrochemistry and heterogeneous catalysis. When oxygen crosses an interface, materials are reduced or oxidized, and it is the strength of reducible oxides that they can absorb and deliver large amounts of oxygen without losing their structural integrity.[1] This phenomenon is known as oxygen storage capacity (OSC),[2] and it is exploited in a wide range of technologies and devices.[3−5] Ceria, as the most prominent reducible oxide, with outstanding importance for the conversion of acid gases in catalytic processes,[6] is used in the water gas shift and hydrocarbon oxidation reactions, and the automotive three-way catalyst is its most popular application.[7−13] Further, ceria-based materials are used for oxide fuel cells, in resistive switching devices and in biological applications.[14−16] Ceria is known to be stabilized in several reduced bulk phases of a rich phase diagram with stoichiometries ranging from CeO_2, in the fully oxidized state, to Ce_2O_3, in the fully reduced state. The detailed atomic structures of intermediate bulk phases with $Ce_{11}O_{20}$, Ce_7O_{12}, and Ce_2O_3 stoichiometry have thoroughly been investigated[17−20] and metastable phases have been discussed.[21] However, exploring the structure of the commonly treated reduced (111) surface of ceria has so far been a story of mystery and surprise. Based on experimental evidence collected by scanning probe imaging, it has, for instance, been claimed that vacancies on CeO_2(111) have a tendency to avoid the very surface layer but rather form a regular array in a subsurface layer effectively yielding a (2×2) surface reconstruction.[22] This claim has been later confirmed by extended theoretical simulation revealing that the spatial localization of both, the oxygen vacancies and the excess electrons left in the system upon vacancy formation are crucial for the stability of vacancy structures.[23] Excess electrons localize at cerium sites reducing Ce^{4+} to Ce^{3+} where the distribution of Ce^{3+} ions has a major impact on the formation of distinct defect structures.[24−28]

Here, we report a systematic atomic-scale cartography of surface structures obtained by noncontact atomic force microscopy (NC-AFM),[29] which we interpret in light of structural modeling and density functional theory (DFT) calculations combined with statistical thermodynamics. We unravel the complete picture of reduced ceria (111) surface structures and develop an understanding of the surface phase diagram, explaining the phenomenon of the coexistence of stable phases in certain temperature ranges, and report the discovery of a new surface phase exhibiting an oblique $(\sqrt{7} \times 3)$R19.1° surface atomic reconstruction. This unusual structure with a Ce_3O_5 stoichiometry cannot be stabilized in bulk form but occurs at the CeO_2(111) surface exposed to ultrahigh vacuum (UHV) at a temperature of about 1020 K. The structure and its stoichiometry smoothly fit into the series of other surface atomic structures

Received: January 30, 2017
Revised: March 8, 2017
Published: March 9, 2017

DOI: 10.1021/acs.jpcc.7b00956
J. Phys. Chem. C 2017, 121, 6844−6851

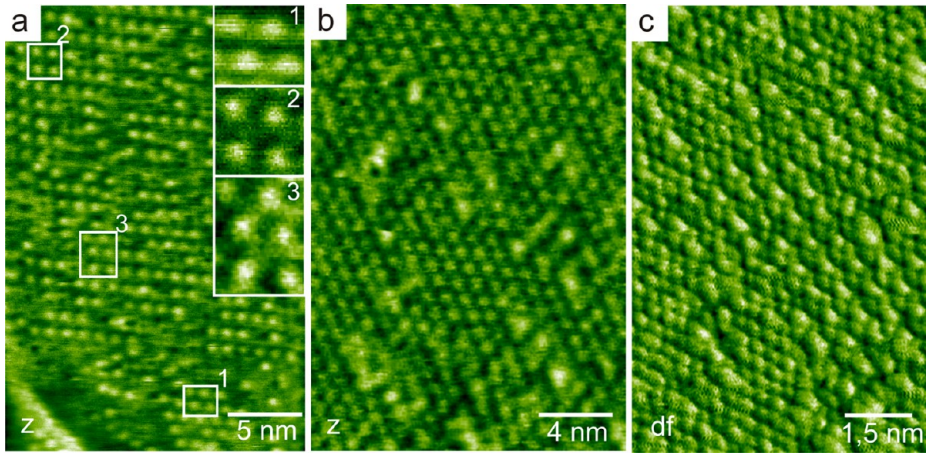

Figure 1. Selected NC-AFM images obtained after annealing at 1020 (frames a and b) to 1050 K (frame c) under UHV conditions representing different phases of the cerium oxide (111) surface. (a) The *ι*-phase exhibiting the $(\sqrt{7} \times \sqrt{7})$R19.1° reconstruction (inset 1) and the oblique structure exhibiting the $(\sqrt{7} \times 3)$R19.1° reconstruction (inset 2) coexist on the same terrace (inset 3). (b) Terrace area purely covered by the *ι*-phase and some contaminants. (c) Terrace showing the $(\sqrt{3} \times \sqrt{3})$R30° reconstruction coexisting with the (1×1) termination. The topographic (*z*) and frequency shift (*df*) images are color coded in corresponding scales: a brighter contrast corresponds to a higher *z* value or a larger frequency shift *df*.

corresponding to known bulk phases that can be produced successively, partially coexisting with each other, by a gradual variation of the chemical potential of gas phase oxygen at the surface. Also, a previously not known $(\sqrt{3} \times \sqrt{3})$R30° reconstruction is reported.

EXPERIMENTAL AND THEORETICAL METHODS

The system investigated is a bulk-like 180 nm thick, high quality ceria film grown on Si(111) by molecular beam epitaxy (MBE) as described in detail in refs 30 and 31. Previous work has shown that the surface prepared in its high temperature phase exhibits atomically well-ordered large terraces with a (1×1) atomic structure and CeO_2 stoichiometry,[32,33] specifically when annealed in oxygen[34] and that the film reduces upon extended heat treatment in vacuum.[35] We choose this surface as the starting point of our investigations and prepare a series of increasingly reduced surfaces by annealing in the ultrahigh vacuum (UHV)[36] at stepwise increased temperature until we again observe a (1×1) atomic structure, but this time with the Ce_2O_3 stoichiometry. To keep thermal stress low, heating and cooling rates are limited to 25 K/min. The set-point temperature is kept for 35 min and the annealing cycles are started at a base pressure well below 10^{-10} mbar.

The NC-AFM imaging is performed with a commercial ultrahigh vacuum AFM/STM (Omicron NanoTechnology, Taunusstein, Germany) operated in the same manner as in previous work,[37−39] but with optimized hardware[40] and well characterized probes and electronics.[41−43] The image contrast presented in the figures is either the apparent topography denoted by *z*, when scanning in the constant frequency shift mode, or the frequency shift *df*, when scanning in the quasi-constant height mode.[37] The quantitative interpretation of the image contrast is not trivial for ceria and, therefore, contrast features are discussed here solely on a phenomenological basis.[39] Note that a quantitative understanding of NC-AFM contrast details is not required for the unambiguous identification of the surface reconstruction, which is the goal of this paper.

To achieve an accurate understanding of the surface reconstructions in relation to the surface stoichiometry, we combine high-resolution NC-AFM imaging with extensive spin-polarized DFT+U calculations (where U is a Hubbard-like term describing the onsite Coulomb interactions). To describe the degree of reduction in relation to the number and arrangement of vacancies, we introduce the parameter $\Theta = N_v/N$ as a measure for the defect concentration, where N_v and N are the number of surface plus subsurface vacancies in the reduced layer and the total number of atoms in a nonreduced oxygen layer of the same cell, respectively. The reduced ceria overlayers on $CeO_2(111)$ are modeled using supercells containing up to six O−Ce−O trilayers (TL) with the calculated CeO_2 bulk equilibrium lattice constant of 0.5485 nm. All but the bottom TL are allowed to relax with the surface unit cell size kept fixed during geometry optimization. Further details of the calculation can be found in refs 19 and 23. Strong correlation effects due to localization are modeled by adding a Hubbard-U term (U_{eff} = 4.5 eV for Ce 4f states) to the energy functional[44,45] expressed in the projected augmented wave (PAW) method within a plane wave approach as implemented in the Vienna ab initio simulation package (VASP).[46] The Perdew−Burke−Ernzerhof (PBE) exchange correlation functional[47] is used. The Brillouin zone is sampled using Monkhorst−Pack k-point meshes ranging from $(2 \times 2 \times 1)$ to $(6 \times 6 \times 1)$, as required by the surface structure periodicities. In the construction of models of reduced ceria overlayers on $CeO_2(111)$ corresponding to commonly found stoichiometries such as Ce_7O_{12} and Ce_2O_3, the distinct location of the vacancies in the corresponding bulk phases has been taken into account.[18,23,48] For all other structures, vacancies are placed such that the closest vacancy distance would correspond to that of second neighbors in the oxygen sublattice (along the ⟨011⟩ direction), favoring the near-surface region, particularly the immediate subsurface oxygen layer,[22,24] and that there would not be neighboring vacancies along the ⟨100⟩ directions of the fluorite lattice. This rule for ordering vacancies has been derived from the crystallographic analysis of reduced bulk ceria phases[18] and has recently been confirmed on the basis of rigorous atomistic modeling.[19] As for the location of the Ce^{3+} ions, preference is given to next-nearest neighbor cation sites relative to the vacancies and a position close to the surface in accordance with recent modeling and experimental results.[23,24,26,28,49]

RESULTS AND DISCUSSION

In frames a and b of Figure 1, we show survey scans obtained after annealing the film at 1020 K and in frame (c), the result after

DOI: 10.1021/acs.jpcc.7b00956
J. Phys. Chem. C 2017, 121, 6844−6851

further annealing at 1050 K. As a typical result for all surfaces not having the (1 × 1) bulk termination, we find that the surface exhibits atomic regularity, however, it is not homogeneously covered by one phase but there are coexisting phases, voids and structural defects. Frame (a) is dominated by regularly arranged structures covering the same terrace in interweaved patches of two phases. A small part of the terrace is covered with a hexagonal structure (inset 1) having a side length of 1 nm. The structure is rotated with respect to the (1 × 1) bulk termination of $CeO_2(111)$ and perfectly matches the known ι-phase exhibiting a $(\sqrt{7} \times \sqrt{7})R19.1°$ reconstruction based on the Ce_7O_{12} stoichiometry.[50] The larger part of the terrace is, however, covered by an unexpected and so far not reported oblique surface structure (inset 2). The structure has a size of 1 nm × 1.15 nm and it is rotated by 19.1° with respect to the unreconstructed $CeO_2(111)$ surface, corresponding to a $(\sqrt{7} \times 3)R19.1°$ superlattice. Close inspection reveals that both structures coexist within small areas and may smoothly merge as evidenced by the image section shown in inset 3. The formation of coexisting phases seems to depend on subtle differences in surface preparation, as for example in frame (b), showing a surface prepared with the same annealing procedure, we observe large patches exclusively exhibiting the ι-phase. This result points to the very similar thermodynamic stability of the two structures.

After repeated annealing and increasing the temperature by 30 K, the $(\sqrt{7} \times 3)R19.1°$ and $(\sqrt{7} \times \sqrt{7})R19.1°$ reconstructions disappear and another so far not reported surface structure is observed. This is presented in frame (c) where we find hexagonally arranged brighter and darker spots with a repeating distance of 0.66 nm. Coexisting with this new structure, we observe the (1 × 1) termination making it easy to assign the hexagonal structure to a $(\sqrt{3} \times \sqrt{3})R30°$ reconstruction. Despite the coexistence of these two phases, the surface does not exhibit apparent voids or vacancies. We interpret the pattern of slightly brighter and darker contrast as features associated with the presence of subsurface oxygen defects. Upon further annealing the film at a temperature of 1080 K, the $(\sqrt{3} \times \sqrt{3})R30°$ reconstruction disappears completely and the surface is solely covered by atoms arranged in a (1 × 1) structure. Noteworthy, its atomic arrangement appears to be identical to the one observed for the fully stoichiometric $CeO_2(111)$ surface;[51] however, the history of reduction suggests that the surface has undergone a phase transition to A-type hexagonal Ce_2O_3 representing the fully reduced state. This means that under UHV conditions, we can transform the surface from the fully oxidized state to the fully reduced state by annealing over a temperature range from 1020 to 1080 K, while the surface passes through a series of atomically well-ordered structures of different stoichiometry.

Figure 2 provides an overview of the five ceria phases observed with NC-AFM and the calculated models of the atomic surface structures yielding the lowest formation energy along with the corresponding unit cells. The NC-AFM image in (a) represents the defect-free, stoichiometric $CeO_2(111)$ surface measured on a bulk crystal. The (1 × 1) surface unit cell has a side length of 0.38 nm along $\langle\bar{1}\,01\rangle$ and, as there are no vacancies, Θ equals 0. The $(\sqrt{7} \times \sqrt{7})R19.1°$ reconstruction or ι-phase is shown in frame (b). A careful comparison to Figure 1 reveals that the ι-phase appears here with its mirror domain.[50] Modeling predicts a Ce_7O_{12} stoichiometry. The surface unit cell contains a net total of two vacancies with surface oxygen vacancies on the cell corners plus one subsurface oxygen vacancy, perfectly matching the NC-AFM image contrast. The surface oxygen vacancies appear as dark contrast features at the corners of the unit cell containing brighter and darker triangular structures. The brighter structures can be resolved into three features associated with oxygen atoms while this is not so apparent for the darker structures. According to the model, the six surface oxygen atoms within the unit cell can be assigned to two triangular structures where the one having a subsurface oxygen vacancy beneath appears with the darker contrast due to downward relaxation. The two vacancies are located in the outermost O−Ce−O trilayer (TL) yielding a Θ value of 2/7. The Ce_7O_{12} bulk structure can be constructed by stacking such TLs. Also, the model for the oblique $(\sqrt{7} \times 3)R19.1°$ reconstruction presented in frame (c) very well matches the NC-AFM image. The topography exhibits four dark spots assigned to the surface oxygen vacancies positioned at unit cell corners. The surface oxygen atoms forming triangles at the periphery of the unit cell appear well separated from each other because oxygen atoms at the center of the unit cell appear darker due to the presence of adjacent subsurface vacancies. The three vacancies are located in the first (top) TL, one in the surface oxygen layer and two subsurface, yielding a Ce_3O_5 stoichiometry and a Θ value of 1/3. The model for the $(\sqrt{3} \times \sqrt{3})R30°$ reconstruction presented in frame (d) predicts vacancies only in subsurface layers, well explaining the low overall contrast of the NC-AFM image. The cell contains a net total of three vacancies, two in the top TL and one in the third TL. While the first cerium layer is exclusively formed by Ce^{3+} ions, two Ce^{4+} ions are found in the second cerium layer. The NC-AFM image exhibits brighter and darker spots where the darker ones appear to be positioned in between the atomic rows of the surface oxygen layer relating them to the subsurface vacancies. Bright spots are positioned exclusively at unit cell corners and we speculate that they are related to the presence of subsurface oxygen atoms bonded to a Ce^{4+} ion in the second cerium layer. The peculiar distribution of three vacancies in the $(\sqrt{3} \times \sqrt{3})R30°$ model structure is consistent with rules for the distribution of vacancies and yields a Ce_3O_5 stoichiometry with a Θ value of 1. The image in frame (e) shows the (1 × 1) termination formed upon annealing at the highest temperature of 1080 K. We anticipate that this is the (0001) surface of hexagonal A-type Ce_2O_3, however, the NC-AFM image contrast cannot be distinguished from the one obtained on (1 × 1) bulk-terminated $CeO_2(111)$.[52] Analyzing the model, we find that the cell contains a net total of two vacancies within the four outermost TLs yielding a Ce_2O_3 stoichiometry and a Θ value of 2. A (0001) oriented Ce_2O_3 bulk crystal can be constructed by stacking such reduced surface oxide layers. Experimentally, we find that this phase cannot be reduced any further by continuing the annealing at even higher temperature.

In our NC-AFM study, we observe the five described surface reconstructions, however, in the literature there are reports on two further variants for reduced ultrathin ceria films, namely the (3 × 3) and (4 × 4) reconstructions.[53,54] To complete the picture of all reduced ceria surface phases, these crystal structures are also modeled by DFT and shown in Figure 3. As the main feature of the (3 × 3) reconstruction presented in frame (a), we find surface oxygen vacancies at the corners of the unit cell while two additional oxygen vacancies per unit cell are placed subsurface. With the three oxygen vacancies within the top TL, Θ is 1/3 and the stoichiometry is Ce_3O_5. The (4 × 4) reconstruction shown in frame (b) represents the completely reduced C-type Ce_2O_3 bixbyite phase and has the largest surface unit cell of all investigated reconstructions. The minimum thickness with a stable (4 × 4) reconstruction is 4 TLs, each having eight

DOI: 10.1021/acs.jpcc.7b00956
J. Phys. Chem. C 2017, 121, 6844−6851

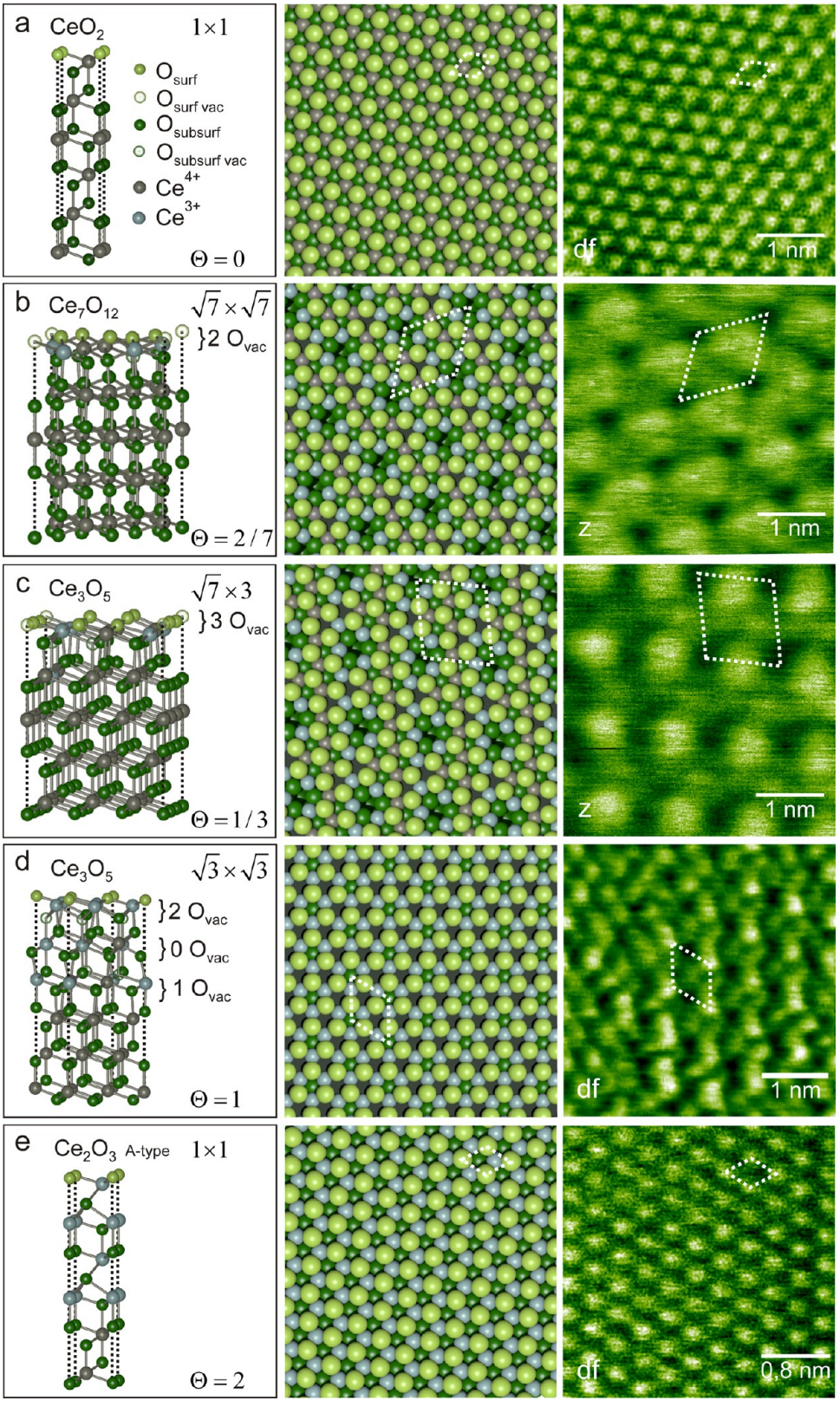

Figure 2. Overview of the ceria phases observed with NC-AFM (right column) and corresponding DFT surface structure models (left and middle columns). Unit cells are marked by dashed lines. (a) (1 × 1) CeO_2; (b) ($\sqrt{7} \times \sqrt{7}$)R19.1° Ce_7O_{12}; (c) ($\sqrt{7} \times 3$)R19.1° Ce_3O_5; (d) ($\sqrt{3} \times \sqrt{3}$)R30° Ce_3O_5; (e) (1 × 1) Ce_2O_3. The color code is the same as the one in Figure 1.

vacancies corresponding to a Θ value of 2. The bulk bixbyite Ce_2O_3 structure can be constructed by stacking such reduced surface oxide layers.

For understanding the surface structures and their stoichiometry in thermal equilibrium under reducing conditions in a vacuum environment, we combine the DFT total energy calculations with

DOI: 10.1021/acs.jpcc.7b00956
J. Phys. Chem. C 2017, 121, 6844−6851

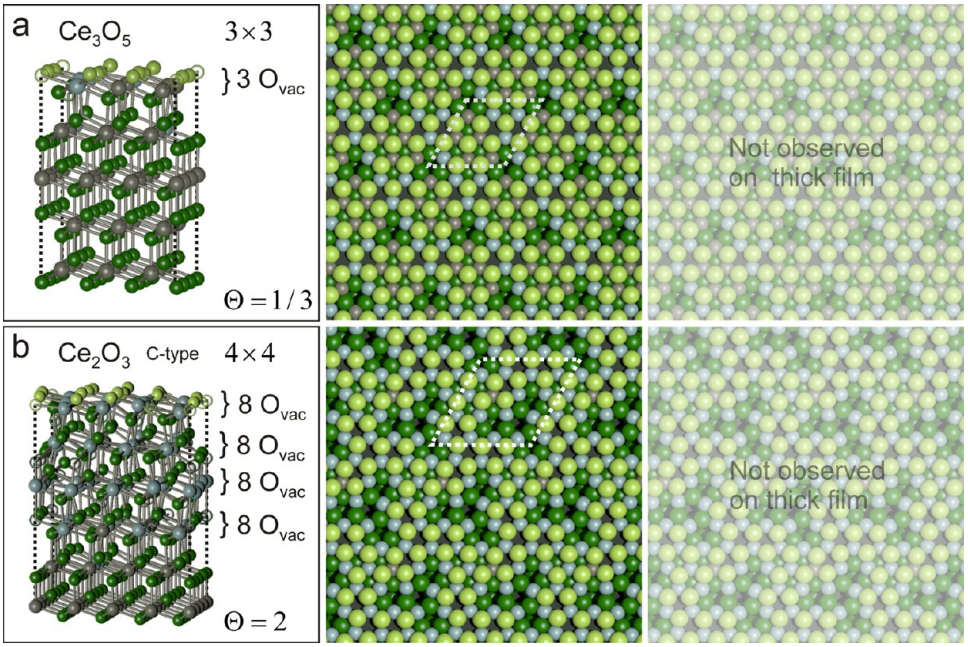

Figure 3. DFT surface structure models of two stable ceria phases that have not been observed in experiments on thick films but only in diffraction studies on thin films.[53−55] (a) (3 × 3) Ce_3O_5; (b) (4 × 4) Ce_2O_3.

statistical thermodynamics.[56,57] We identify thermodynamically stable structures at a given temperature T and molecular oxygen partial pressure p_{O_2} by the change in the surface free energy upon surface reduction $\Delta\gamma(T,p_{O_2},\Theta) = N_v/A[E_v(\Theta) + \Delta\mu_O(T,p_{O_2})]$, as outlined in refs 23 and 58. The quantities N_v, A, and E_v, are the number of vacancies, the area of the surface unit cell, and the average vacancy formation energy, respectively. $\Delta\mu_O(T,p_{O_2}) = 1/2[\mu_{O_2}(T,p_{O_2}) - E_{O_2}]$, is the change of the oxygen chemical potential, where the total energy E_{O_2} of an isolated molecule at T = 0 K is taken as the reference state.

Figure 4 shows the results for the most stable surface structures with vacancy concentrations ranging from Θ = 0 to Θ = 2, where the change in surface free energy $\Delta\gamma$ is displayed as a function of the change in oxygen chemical potential $\Delta\mu_O$. The thermodynamically favored phase at a given $\Delta\mu_O$ is the one for which $\Delta\gamma$ ($\Delta\gamma$ < 0) is largest in magnitude. In the top x-axis, $\Delta\mu_O$ is translated into a temperature scale at an oxygen partial pressure of 10^{-8} mbar, assuming ideal gas behavior and using tabulated values for the enthalpy and entropy of O_2 as a function of T at standard pressure.[59] The 10^{-8} mbar pressure value has been chosen pragmatically as a best fit to experimentally observed surface stabilization at given temperatures. It cannot be further justified as it is experimentally not possible to measure the oxygen pressure in the region directly above the hot sample surface. The stability plot in Figure 4 yields a perfectly consistent picture as it reproduces the sequence of surface reconstructions experimentally observed upon temperature variation and the order follows the degree of reduction expressed by the parameter Θ. Upon increasing the annealing temperature, the first reconstructions that appear are those corresponding to Θ = 1/16, 1/8 and 1/4, namely, isolated subsurface vacancies, pairs of third-neighbor subsurface vacancies, and the (2 × 2) structure of an extended subsurface vacancy layer that we previously identified in NC-AFM measurements[22] and confirmed by DFT calculations and thermodynamic analysis.[23] The next structure is the $(\sqrt{7}\times\sqrt{7})$R19.1° reconstruction with a vacancy concentration

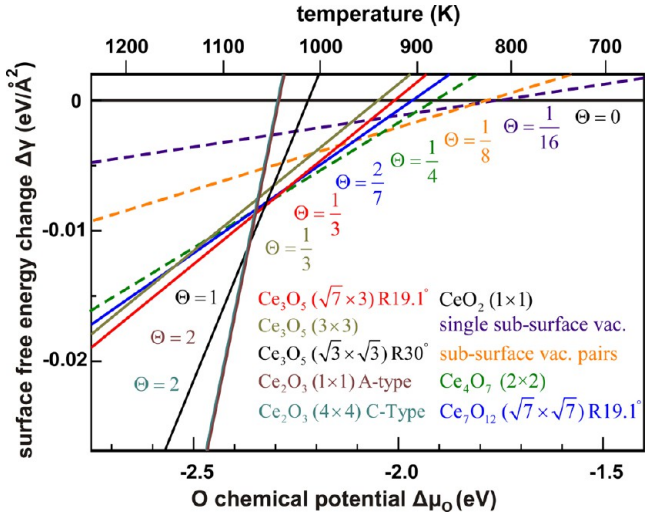

Figure 4. Stability plot for the ceria surface phases obtained by DFT and thermodynamic modeling. The change in surface free energy is plotted as a function of the oxygen chemical potential $\Delta\mu_O(T,p_{O_2})$. To generate the top x-axis, $\Delta\mu_O$ is translated into a temperature T, assuming an oxygen partial pressure p_{O_2} of 10^{-8} mbar, as described in the main text. The dashed lines for Θ = 1/16, 1/8, and 1/4 correspond to previously reported isolated subsurface defects, vacancy pairs, and the (2 × 2) structure of ordered subsurface vacancies.[23]

of Θ = 2/7 that is quite stable over a relatively wide range of reducing conditions but competes with the structures at Θ = 1/4 and Θ = 1/3. The closeness of the lines for the $(\sqrt{7}\times\sqrt{7})$R19.1° and $(\sqrt{7}\times 3)$R19.1° reconstructions readily explains the coexistence of these phases found in NC-AFM experiments. The next phase appearing with increasing temperature is the $(\sqrt{3}\times\sqrt{3})$R30° phase with Θ = 1. The calculation clearly predicts that this phase is more stable than the $(\sqrt{7}\times\sqrt{7})$R19.1° phase in a small temperature interval above 1040 K, in agreement with the experimental observation. At higher temperatures, the

DOI: 10.1021/acs.jpcc.7b00956
J. Phys. Chem. C 2017, 121, 6844−6851

(1×1) and (4×4) phases with $\Theta = 2$ are equally well stabilized, while in the NC-AFM experiment only the (1×1) phase is observed.

The absence of the (3×3) reconstruction in the NC-AFM experiments can be readily explained. Careful annealing with small temporal temperature gradients ensures a surface stabilization close to the thermodynamic equilibrium and excludes the formation of a reconstruction with a surface free energy that is never among the lowest ones over the entire temperature range as it is evident from the stability plot of Figure 4. However, the (3×3) reconstruction has been observed in diffraction experiments on ceria thin films grown on Ru(0001) after surface reduction by hydrogen exposure.[54] In these experiments, samples are heated to temperatures not higher than 700 K and the reduction is facilitated by a surface chemical reaction. Interestingly, hydrogen reduction experiments also favor the formation of the (4×4) phase, while the ι-phase is not observed. Furthermore, the (3×3) and (4×4) phases have been observed in ceria thin films grown on Cu(111) and Pt(111), where the reduction has been ascribed to an interfacial reaction with metallic cerium[53] or the stabilization of the surface phase is subscribed to the influence of the substrate.[60] These results highlight that reduction for ultrathin films is likely to be controlled by the interface opposite to the interaction between the surface and the bulk reservoir of oxygen and vacancies present for the systems investigated here.

Overall, we find that all reconstructions experimentally observed can be straightforwardly ascribed to stable structures predicted by DFT calculations. Most notably, our calculations predict a stabilization of the surface in the unusual Ce_3O_5 stoichiometry. Modeling reduced ceria layers with the Ce_3O_5 stoichiometry on a $CeO_2(111)$ bulk terminated surface in suitable ways, results in three different surface phases. Two of them, namely the (3×3) and the $(\sqrt{3} \times \sqrt{3})R30°$ phases exhibit a vacancy structure that would allow a stacking of the respective Ce_3O_5 surface layers to form a Ce_3O_5 bulk crystal structure, according to the rules for the ordering of oxygen vacancies.[18,19] However, the oblique $(\sqrt{7} \times 3)R19.1°$ surface phase is unique and can only exist as a thin reduced oxide layer, because hypothetically stacking such layers to form a bulk crystal would yield neighboring vacancies along the $\langle 100 \rangle$ directions in the fluorite lattice that are forbidden according to the mentioned vacancy ordering rules. Significantly, we find that the average defect formation energy of the oblique $(\sqrt{7} \times 3)R19.1°$ phase is 40 meV per vacancy lower than that for the (3×3) reconstruction. The average vacancy formation energies of the unrelaxed structures are similar. Hence, the increased stability is likely due to cooperative lattice relaxation effects that accompany the formation of the distinct vacancy arrangement and the identified localization of the excess charge. Thus, the $(\sqrt{7} \times 3)R19°$ reduced ceria phase is favored under thermal equilibrium conditions but it is likely to coexist with the somewhat less reduced $(\sqrt{7} \times \sqrt{7})R19.1°$ phase with nanosized domains as observed in experiment. Upon further reduction, phases such as the $(\sqrt{3} \times \sqrt{3})R30°$ and the fully reduced (1×1) structure are formed.

CONCLUSION

Our work shows that structural relaxations accompanying oxygen release from ceria and the localization of the excess charge are crucial for the stabilization of ordered arrangements of vacancies on the surface of reduced ceria. Moreover, as the reduced surface layer increases in thickness, oxygen defects, and associated Ce^{3+} ions are found to obey ordering rules known for reduced bulk phases that we here establish as overarching construction principles for reduced ceria. Our observations shed light on structures that could be stabilized when growing ultrathin ceria films on metal or semiconducting substrates. So far, surface atomic arrangements have been reported for a few systems only.[53,61−63] The present work and its precursors clearly demonstrate that the prediction and understanding of novel surface structures invariably requires the combination of state-of-the-art structural characterization with rigorous atomistic modeling, including precise calculations for a large set of explorative models for the placement of oxygen vacancies and Ce^{3+} ions in the crystal lattice. Knowing the surface defect structure including the location of defects and Ce^{3+} ions is of paramount importance for the application of ceria in real devices because it governs the physics and chemistry of reduced phases. For example, defects are expected to serve as anchoring sites for metal nanoparticles in metal/ceria catalysts[64] and to influence the structure and charge of supported metal clusters,[65] while Ce^{3+} centers are typically an important part of the active site.[66] The fundamental understanding of ceria surface defect structures opens doors for exploiting and tailoring ceria-based systems functionality, particularly in electrochemical and catalytic processes.

AUTHOR INFORMATION

Corresponding Authors

*E-mail: reichling@uos.de.

*E-mail: vgp@icp.csic.es.

ORCID

Reinhard Olbrich: 0000-0001-7765-393X

Author Contributions

‡These authors contributed equally to this work.

Notes

The authors declare no competing financial interest.

ACKNOWLEDGMENTS

We are grateful to G. Niu, M. H. Zoellner, and T. Schroeder from the IHP, Frankfurt (Oder), Germany, for sample preparation. We thank ANPCyT (Grant Nos. PICT-1555, PICT-1857, and PICT-1187), CONICET-Argentina (Grant No. PIP-0069CO), and MINECO-Spain (CTQ2012-32928 and CTQ2015-71823-R) for financial support. Computer time provided by the SGAI-CSIC, CESGA, BSC, University of Cantabria-IFCA, and BIFI-ZCAM and support from the COST Action CM1104 is gratefully acknowledged.

REFERENCES

(1) Feng, Z. L. A.; El Gabaly, F.; Ye, X. F.; Shen, Z. X.; Chueh, W. C. Fast Vacancy-Mediated Oxygen Ion Incorporation Across the Ceria-Gas Electrochemical Interface. *Nat. Commun.* **2014**, *5*, 4374−4382.

(2) Balducci, G.; Islam, M. S.; Kaspar, J.; Fornasiero, P.; Graziani, M. Bulk Reduction and Oxygen Migration in the Ceria-Based Oxides. *Chem. Mater.* **2000**, *12*, 677−681.

(3) Yao, H. C.; Yao, Y. F. Y. Ceria in Automotive Exhaust Catalysts: I. Oxygen Storage. *J. Catal.* **1984**, *86*, 254−265.

(4) Di Monte, R.; Kaspar, J. On the Role of Oxygen Storage in Three-Way Catalysis. *Top. Catal.* **2004**, *28*, 47−57.

(5) Montini, T.; Melchionna, M.; Monai, M.; Fornasiero, P. Fundamentals and Catalytic Applications of CeO_2-Based Materials. *Chem. Rev.* **2016**, *116*, 5987−6041.

DOI: 10.1021/acs.jpcc.7b00956
J. Phys. Chem. C 2017, 121, 6844−6851

(6) Tumuluri, U.; Rother, G.; Wu, Z. L. Fundamental Understanding of the Interaction of Acid Gases with CeO_2: From Surface Science to Practical Catalysis. *Ind. Eng. Chem. Res.* **2016**, *55*, 3909−3919.
(7) Conesa, J. C.; Martìnez-Arias, A.; Fernàndez-Garcìa, M.; Soria, J. Surface Structure and Redox Chemistry of Ceria-Containing Automotive Catalytic Systems. *Res. Chem. Intermed.* **2000**, *26*, 103−111.
(8) Gandhi, H. S.; Graham, G. W.; McCabe, R. W. Automotive Exhaust Catalysis. *J. Catal.* **2003**, *216*, 433−442.
(9) Gorte, R. J. Ceria in Catalysis: From Automotive Applications to the Water Gas Shift Reaction. *AIChE J.* **2010**, *56*, 1126−1135.
(10) Yao, S. Y.; Xu, W. Q.; Johnston-Peck, A. C.; Zhao, F. Z.; Liu, Z. Y.; Luo, S.; Senanayake, S. D.; Martinez-Arias, A.; Liu, W. J.; Rodriguez, J. A. Morphological Effects of the Nanostructured Ceria Support on the Activity and Stability of CuO/CeO_2 Catalysts for the Water-Gas Shift Reaction. *Phys. Chem. Chem. Phys.* **2014**, *16*, 17183−17195.
(11) Trovarelli, A.; Fornasiero, P. *Catalysis by Ceria and Related Materials*, 2nd ed.; Imperial College Press: London, 2013.
(12) Hilaire, S.; Wang, X.; Luo, T.; Gorte, R.; J, W. A Comparative Study of Water-Gas-Shift Reaction Over Ceria-Supported Metallic Catalysts. *Appl. Catal., A* **2001**, *215*, 271−278.
(13) Kovacevic, M.; Mojet, B. L.; van Ommen, J. G.; Lefferts, L. Effects of Morphology of Cerium Oxide Catalysts for Reverse Water Gas Shift Reaction. *Catal. Lett.* **2016**, *146*, 770−777.
(14) Park, S. D.; Vohs, J. M.; Gorte, R. J. Direct Oxidation of Hydrocarbons in a Solid-Oxide Fuel Cell. *Nature* **2000**, *404*, 265−267.
(15) Miranda, E.; Kano, S.; Dou, C.; Kakushima, K.; Sune, J.; Iwai, H. Nonlinear Conductance Quantization Effects in CeO_x/SiO_2-Based Resistive Switching Devices. *Appl. Phys. Lett.* **2012**, *101*, 12910−12913.
(16) Xu, C.; Qu, X. Cerium Oxide Nanoparticle: A Remarkably Versatile Rare Earth Nanomaterial for Biological Applications. *NPG Asia Mater.* **2014**, *6*, e90−e105.
(17) Adachi, G.; Imanaka, N. The binary rare earth oxides. *Chem. Rev.* **1998**, *98*, 1479−1514.
(18) Kümmerle, E. A.; Heger, G. The structures of C-Ce_2O_{3+d}, Ce_7O_{12}, and $Ce_{11}O_{20}$. *J. Solid State Chem.* **1999**, *147*, 485−500.
(19) Murgida, G. E.; Ferrari, V.; Ganduglia-Pirovano, M. V.; Llois, A. M. Ordering of Oxygen Vacancies and Excess Charge Localization in Bulk Ceria: A DFT+*U* Study. *Phys. Rev. B: Condens. Matter Mater. Phys.* **2014**, *90*, 115120−115131.
(20) Ricken, M.; Nölting, J.; Riess, I. Specific Heat and Phase Diagram of Nonstoichiometric Ceria (CeO_{2-x}). *J. Solid State Chem.* **1984**, *54*, 89−99.
(21) Eyring, L. In *Synthesis of Lanthanide and Actinide Compounds*; Meyer, G., Morss, L. R., Eds.; Springer: Netherlands, 1991; pp 187−224.
(22) Torbrügge, S.; Reichling, M.; Ishiyama, A.; Morita, S.; Custance, O. Evidence of Subsurface Oxygen Vacancy Ordering on Reduced $CeO_2(111)$. *Phys. Rev. Lett.* **2007**, *99*, 56101−56105.
(23) Murgida, G. E.; Ganduglia-Pirovano, M. V. Evidence for Subsurface Ordering of Oxygen Vacancies on the Reduced $CeO_2(111)$ Surface Using Density-Functional and Statistical Calculations. *Phys. Rev. Lett.* **2013**, *110*, 246101−246105.
(24) Ganduglia-Pirovano, M. V.; da Silva, J. L. F.; Sauer, J. Density-Functional Calculations of the Structure of Near-Surface Oxygen Vacancies and Electron Localization on $CeO_2(111)$. *Phys. Rev. Lett.* **2009**, *102*, 26101−26105.
(25) Migani, A.; Vayssilov, G. N.; Bromley, S. T.; Illas, F.; Neyman, K. M. Greatly Facilitated Oxygen Vacancy Formation in Ceria Nanocrystallites. *Chem. Commun.* **2010**, *46*, 5936−5938.
(26) Jerratsch, J. F.; Shao, X.; Nilius, N.; Freund, H. J.; Popa, C.; Ganduglia-Pirovano, M. V.; Burow, A. M.; Sauer, J. Electron Localization in Defective Ceria Films: A Study with Scanning-Tunneling Microscopy and Density-Functional Theory. *Phys. Rev. Lett.* **2011**, *106*, 246801−246804.
(27) Sk, M. A.; Kozlov, S. M.; Lim, K. H.; Migani, A.; Neyman, K. M. Oxygen vacancies in Self-Assemblies of Ceria Nanoparticles. *J. Mater. Chem. A* **2014**, *2*, 18329−18338.
(28) Sutton, J. E.; Beste, A.; Overbury, S. H. Origins and Implications of the Ordering of Oxygen Vacancies and Localized Electrons on Partially Reduced $CeO_2(111)$. *Phys. Rev. B: Condens. Matter Mater. Phys.* **2015**, *92*, 144105−144112.
(29) Lauritsen, J. V.; Reichling, M. Atomic Resolution Non-Contact Atomic Force Microscopy of Clean Metal Oxide Surfaces. *J. Phys.: Condens. Matter* **2010**, *22*, 263001−263023.
(30) Niu, G.; Zoellner, M. H.; Schroeder, T.; Schaefer, A.; Jhang, J. H.; Zielasek, V.; Bäumer, M.; Wilkens, H.; Wollschläger, J.; Olbrich, R.; et al. Controlling the Physics and Chemistry of Binary and Ternary Praseodymium and Cerium Oxide Systems. *Phys. Chem. Chem. Phys.* **2015**, *17*, 24513−24540.
(31) Zoellner, M. H.; Dabrowski, J.; Zaumseil, P.; Giussani, A.; Schubert, M. A.; Lupina, G.; Wilkens, H.; Wollschläger, J.; Reichling, M.; Bäumer, M.; et al. Stacking Behavior of Twin-Free Type-B Oriented $CeO_2(111)$ Films on Hexagonal $Pr_2O_3(0001)/Si(111)$ Systems. *Phys. Rev. B: Condens. Matter Mater. Phys.* **2012**, *85*, 35302−35310.
(32) Olbrich, R.; Pieper, H. H.; Oelke, R.; Wilkens, H.; Wollschläger, J.; Zoellner, M. H.; Schroeder, T.; Reichling, M. A Well-Structured Metastable Ceria Surface. *Appl. Phys. Lett.* **2014**, *104*, 81910−81915.
(33) Pieper, H. H.; Derks, C.; Zoellner, M. H.; Olbrich, R.; Tröger, L.; Schroeder, T.; Neumann, M.; Reichling, M. Morphology and Nanostructure of $CeO_2(111)$ Surfaces of Single Crystals and Si(111) Supported Ceria Films. *Phys. Chem. Chem. Phys.* **2012**, *14*, 15361−15368.
(34) Barth, C.; Laffon, C.; Olbrich, R.; Ranguis, A.; Parent, P.; Reichling, M. A Perfectly Stoichiometric and Flat $CeO_2(111)$ Surface on a Bulk-Like Ceria Film. *Sci. Rep.* **2016**, *6*, 21165−21171.
(35) Wilkens, H.; Schuckmann, O.; Oelke, R.; Gevers, S.; Reichling, M.; Schaefer, A.; Bäumer, M.; Zoellner, M. H.; Niu, G.; Schroeder, T.; et al. Structural Transitions of Epitaxial Ceria Films on Si(111). *Phys. Chem. Chem. Phys.* **2013**, *15*, 18589−18599.
(36) Pieper, H. H.; Lammers, C.; Tröger, L.; Bahr, S.; Reichling, M. Versatile System for the Temperature-Controlled Preparation of Oxide Crystal Surfaces. *Rev. Sci. Instrum.* **2012**, *83*, 55110−55114.
(37) Gritschneder, S.; Namai, Y.; Iwasawa, Y.; Reichling, M. Structural Features of $CeO_2(111)$ Revealed by Dynamic SFM. *Nanotechnology* **2005**, *16*, S41−S48.
(38) Gritschneder, S.; Reichling, M. Structural Elements of $CeO_2(111)$ Surfaces. *Nanotechnology* **2007**, *18*, 44024−44029.
(39) Gritschneder, S.; Reichling, M. Atomic Resolution Imaging on $CeO_2(111)$ with Hydroxylated Probes. *J. Phys. Chem. C* **2008**, *112*, 2045−2049.
(40) Torbrügge, S.; Lübbe, J.; Tröger, L.; Cranney, M.; Eguchi, T.; Hasegawa, Y.; Reichling, M. Improvement of a Dynamic Scanning Force Microscope for Highest Resolution Imaging in Ultrahigh Vacuum. *Rev. Sci. Instrum.* **2008**, *79*, 83701−83708.
(41) Lübbe, J.; Tröger, L.; Torbrügge, S.; Bechstein, R.; Richter, C.; Kühnle, A.; Reichling, M. Achieving High Effective Q-factors in Ultra-High Vacuum Dynamic Force Microscopy. *Meas. Sci. Technol.* **2010**, *21*, 125501−125509.
(42) Lübbe, J.; Doering, L.; Reichling, M. Precise Determination of Force Microscopy Cantilever Stiffness from Dimensions and Eigenfrequencies. *Meas. Sci. Technol.* **2012**, *23*, 45401−45409.
(43) Lübbe, J.; Temmen, M.; Rode, S.; Rahe, P.; Kühnle, A.; Reichling, M. Thermal Noise Limit for Ultra-High Vacuum Noncontact Atomic Force Microscopy. *Beilstein J. Nanotechnol.* **2013**, *4*, 32−44.
(44) Cococcioni, M.; de Gironcoli, S. Linear Response Approach to the Calculation of the Effective Interaction Parameters in the LDA+U Method. *Phys. Rev. B: Condens. Matter Mater. Phys.* **2005**, *71*, 35105−35120.
(45) Fabris, S.; Vicario, G.; Balducci, G.; de Gironcoli, S.; Baroni, S. Electronic and Atomistic Structures of Clean and Reduced Ceria Surfaces. *J. Phys. Chem. B* **2005**, *109*, 22860−22867.
(46) Kresse, G.; Furthmüller, J. Efficient Iterative Schemes for Ab Initio Total-Energy Calculations Using a Plane-Wave Basis Set. *Phys. Rev. B: Condens. Matter Mater. Phys.* **1996**, *54*, 11169−11186.
(47) Perdew, J. P.; Burke, K.; Ernzerhof, M. Generalized Gradient Approximation Made Simple. *Phys. Rev. Lett.* **1996**, *77*, 3865−3868.
(48) Bevan, D. J. M.; Martin, R. L. The Role of the Coordination Defect: A New Structural Description of Four Fluorite-Related

DOI: 10.1021/acs.jpcc.7b00956
J. Phys. Chem. C 2017, 121, 6844−6851

Sesquioxide Minerals, Bixbyite (Mn_2O_3), Braunite (Mn_7SiO_{12}), Braunite II ($CaMn_{14}SiO_{24}$), Parwelite ($Mn_{10}Sb_2AS_2Si_2O_{24}$), and their Structural Relationships. *J. Solid State Chem.* **2008**, *181*, 2250−2259.
(49) Li, H. Y.; Wang, H. F.; Gong, X. Q.; Guo, Y. L.; Guo, Y.; Lu, G. Z.; Hu, P. Multiple Configurations of the Two Excess 4f Electrons on Defective CeO_2(111): Origin and Implications. *Phys. Rev. B: Condens. Matter Mater. Phys.* **2009**, *79*, 193401−193405.
(50) Wilkens, H.; Schuckmann, O.; Oelke, R.; Gevers, S.; Schaefer, A.; Bäumer, M.; Zoellner, M. H.; Schroeder, T.; Wollschläger, J. Stabilization of the Ceria Iota-Phase (Ce_7O_{12}) Surface on Si(111). *Appl. Phys. Lett.* **2013**, *102*, 111602−111605.
(51) Torbrügge, S.; Cranney, M.; Reichling, M. Morphology of Step Structures on CeO_2(111). *Appl. Phys. Lett.* **2008**, *93*, 73112−73114.
(52) Da Silva, J. L. F. Stability of the Ce_2O_3 Phases: A DFT+U Investigation. *Phys. Rev. B* **2007**, *76*, 193108−193111.
(53) Duchoň, T.; Dvořák, F.; Aulická, M.; Stetsovych, V.; Vorokhta, M.; Mazur, D.; Veltruská, K.; Skála, T.; Mysliveček, J.; Matolínová, I.; et al. Ordered Phases of Reduced Ceria As Epitaxial Films on Cu(111). *J. Phys. Chem. C* **2014**, *118*, 357−365.
(54) Höcker, J.; Menteş, T. O.; Sala, A.; Locatelli, A.; Schmidt, T.; Falta, J.; Senanayake, S. D.; Flege, J. I. Unraveling the Dynamic Nanoscale Reducibility ($Ce^{4+} \rightarrow Ce^{3+}$) of CeO_x-Ru in Hydrogen Activation. *Adv. Mater. Interfaces* **2015**, *2*, 1500314−1500319.
(55) Duchoň, T.; Dvořák, F.; Aulická, M.; Stetsovych, V.; Vorokhta, M.; Mazur, D.; Veltruská, K.; Skála, T.; Mysliveček, J.; Matolínová, I.; et al. Comment on "Ordered Phases of Reduced Ceria as Epitaxial Films on Cu(111)". *J. Phys. Chem. C* **2014**, *118*, 5058−5059.
(56) Reuter, K.; Scheffler, M. Composition, Structure, and Stability of RuO_2(110) as a Function of Oxygen Pressure. *Phys. Rev. B: Condens. Matter Mater. Phys.* **2001**, *65*, 35406−35416. Errata: Phys. Rev. B 75, 49901 (2007).
(57) Reuter, K.; Scheffler, M. Erratum: Composition, Structure, and Stability of RuO_2(110) as a Function of Oxygen Pressure. *Phys. Rev. B: Condens. Matter Mater. Phys.* **2007**, *75*, 49901−49901.
(58) Ganduglia-Pirovano, M. V.; Sauer, J. Stability of Reduced V_2O_5(001) Surfaces. *Phys. Rev. B: Condens. Matter Mater. Phys.* **2004**, *70*, 45422−45434.
(59) Lide, D. R.; Frederikse, H. *CRC Handbook of Chemistry and Physics*, 83rd ed.; CRC Press: Boca Raton, FL, 2003.
(60) Luches, P.; Pagliuca, F.; Valeri, S. Structural and Morphological Modifications of Thermally Reduced Cerium Oxide Ultrathin Epitaxial Films on Pt(111). *Phys. Chem. Chem. Phys.* **2014**, *16*, 18848−18857.
(61) Grinter, D. C.; Ithnin, R.; Pang, C. L.; Thornton, G. Defect Structure of Ultrathin Ceria Films on Pt(111): Atomic Views from Scanning Tunnelling Microscopy. *J. Phys. Chem. C* **2010**, *114*, 17036−17041.
(62) Hasegawa, T.; Shahed, S. M. F.; Sainoo, Y.; Beniya, A.; Isomura, N.; Watanabe, Y.; Komeda, T. Epitaxial Growth of CeO_2(111) Film on Ru(0001): Scanning Tunneling Microscopy (STM) and X-Ray Photoemission Spectroscopy (XPS) Study. *J. Chem. Phys.* **2014**, *140*, 044711−044718.
(63) Mysliveček, J.; Matolín, V.; Matolínová, I. Heteroepitaxy of Cerium Oxide Thin Films on Cu(111). *Materials* **2015**, *8*, 6346−6359.
(64) Wang, X.; Chen, B.; Chen, G.; Sun, X. Oxygen Vacancies Dependent Au Nanoparticle Deposition and CO Oxidation. *RSC Adv.* **2016**, *6*, 87978−87987.
(65) Rodriguez, J. A.; Ma, S.; Liu, P.; Hrbek, J.; Evans, J.; Pérez, M. Activity of CeO_x and TiO_x Nanoparticles Grown on Au(111) in the Water-Gas Shift Reaction. *Science* **2007**, *318*, 1757−1760.
(66) Lustemberg, P. G.; Ramírez, P. J.; Liu, Z.; Gutiérrez, R. A.; Grinter, D. G.; Carrasco, J.; Senanayake, S. D.; Rodriguez, J. A.; Ganduglia-Pirovano, M. V. Room-Temperature Activation of Methane and Dry Reforming with CO_2 on Ni-CeO_2(111) Surfaces: Effect of Ce^{3+} Sites and Metal-Support Interactions on C-H Bond Cleavage. *ACS Catal.* **2016**, *6*, 8184−8191.

DOI: 10.1021/acs.jpcc.7b00956
J. Phys. Chem. C 2017, 121, 6844−6851